Control of Giant Topological Magnetic Moment and Valley Splitting in Trilayer Graphene

DOI:
10.1103/PhysRevLett.127.136402

Control of Giant Topological Magnetic Moment and Valley Splitting in Trilayer Graphene

Zhehao Ge[1,*], Sergey Slizovskiy[2,3,*], Fredric Joucken[1], Eberth A. Quezada[1], Takashi Taniguchi[4], Kenji Watanabe[5], Vladimir I. Fal'ko[2,3,6,†], Jairo Velasco Jr.[1, †]

[1]*Department of Physics, University of California, Santa Cruz, California, USA*

[2]*Department of Physics and Astronomy, University of Manchester, Oxford Road, Manchester, M13 9PL, UK*

[3]*National Graphene Institute, University of Manchester, Booth Street East, Manchester, M13 9PL UK*

[4]*International Center for Materials Nanoarchitectronics National Institute for Materials Science, 1-1 Namiki, Tsukuba, 305-0044, Japan*

[5] *Research Center for Functional Materials National Institute for Materials Science, 1-1 Namiki, Tsukuba, 305-0044, Japan*

[6] *Henry Royce Institute for Advanced Materials, Manchester, M13 9PL, UK*

[*]These authors contributed equally to this manuscript.
[†]Email: jvelasc5@ucsc.edu, Vladimir.Falko@manchester.ac.uk

Abstract:

Bloch states of electrons in honeycomb two-dimensional crystals with multi-valley band structure and broken inversion symmetry have orbital magnetic moments of a topological nature. In crystals with two degenerate valleys, a perpendicular magnetic field lifts the valley degeneracy *via* a Zeeman effect due to these magnetic moments, leading to magnetoelectric effects which can be leveraged for creating valleytronic devices. In this work, we demonstrate that trilayer graphene with Bernal stacking, (ABA TLG) hosts topological magnetic moments with a large and widely tunable valley g-factor (g_v), reaching a value g_v~500 at the extreme of the studied parametric range. The reported experiment consists in sublattice-resolved scanning tunneling spectroscopy under perpendicular electric and magnetic fields that control the TLG bands. The tunneling spectra agree very well with the results of theoretical modelling that includes the full details of the TLG tight-binding model and accounts for a quantum-dot-like potential profile formed electrostatically under the scanning tunneling microscope tip. Our results show that ABA TLG is a compelling quantum material platform.

The orbital magnetic moment stemming from the rotational motion of electrons is ubiquitous in nature. It can be found in a variety of systems from single atoms to complex crystals, and can influence the magnetic properties of these systems. In recent years, topological magnetic moments emerging from self-rotating wave packets[1] have been discovered in 2D Van der Waals crystals with broken inversion symmetry.[2-6] Experimental manifestations of the topological magnetic moments have been observed recently, including the valley Zeeman effect,[2-16] spontaneous orbital ferromagnetism,[17,18] and orbital magnetoelectric effects.[19-21] The former is important for valleytronics because it enables control of individual valley states, while the latter two could potentially facilitate new ultra-low power magnetic devices. To harness the valley Zeeman and orbital magnetoelectric effects in 2D crystals, systems with topological magnetic moments both large and tunable *via* gate modulation are desirable. The possibility to achieve these properties have been separately demonstrated with Bernal stacked bilayer graphene (BLG,) offering[22] a tunable $g_v \sim 40 - 120$, and moiré superlattices in graphene, with[4] large g_v ~ 2500.

Here we realize a giant gate-tunable topological magnetic moment in naturally occurring Bernal stacked trilayer graphene (ABA TLG) by utilizing its peculiar band structure. The feature of ABA trilayers is that, due to the mirror symmetry of their structure, Fig. 1a, electronic spectra can be viewed as an overlapping 'bilayer' and weakly gapped monolayer[23] (Fig. 1c), with gaps and mutual alignment of the two tunable by the encapsulation environment, gating and doping, illustrated in Fig. 1b. This feature offers an opportunity to engage states with a large topological magnetic moment and therefore giant g_v specific for weakly gapped monolayers.[1,4,6]

In this work we use scanning tunneling microscopy/spectroscopy (STM/STS) to measure this giant g_v and study the tunable topological magnetic moments of the effective MLG band in ABA TLG. The ABA TLG/hBN heterostructure for our STS study is fabricated with a conventional polymer-based transfer method[24] (see supporting information section S1 for sample fabrication details). ABA TLG and hBN are misaligned intentionally to avoid moiré effects. The measurement setup for our experiments is shown in the upper panel of Fig. 2a. The STM tip is grounded, and a bias voltage V_S is applied between the STM tip and ABA TLG to induce a tunneling current. In addition, a backgate voltage V_G is applied between the doped silicon and ABA TLG to institute an out-of-plane electric field that shifts the TLG Fermi energy and modifies the TLG band structure.[25] To avoid interference from adsorbates we performed all STS measurements at the centers of atomically pristine regions that were no smaller than $20 \times 20\ \mathrm{nm}^2$. The lower panel of Fig. 2a shows a typical topography at the center of such a region where the tunneling spectra were acquired. A clear triangular lattice is visible, which agrees with prior STM studies of ABA TLG supported on metals and SiC.[26,27] Furthermore, no moiré pattern is observed in our topography scans, thus indicating the ABA TLG and hBN are indeed misaligned.

A model atomic structure is overlaid on top of the measured topography in Fig. 2a to enable identification of the ABA TLG sublattices. The grey spot corresponds to sublattice A_1 where only the effective MLG states exist, and the bright spot corresponds to sublattice B_1 where both the effective MLG and BLG states exist. Both of these sublattices reside on the top layer, as shown in Fig. 1a. In contrast, the dark spot corresponds to sublattice A_2, which resides on the middle layer. Since STM is mostly sensitive to surface states, we expect the tunneling signal from our measurements to consist primarily of contributions from the top ABA TLG layer, hence sublattices A_1 and B_1 will dominate our STS measurements.

Typical gate and sublattice resolved STS results are shown in Figs. 2b and 2c for sublattices A_1 and B_1, respectively. To reduce the influence of slight deviations from the target sublattice for a single measurement, the tunneling spectra at each gate voltage shown in Figs. 2b and 2c correspond to an average of spectra at nine different targeted locations (see supporting information section S3 for the STS results before averaging). Interestingly, the spectra for sublattice A_1 exhibit a prominent dI/dV_S peak (marked by a black dot) that diminishes in intensity and shifts toward the positive bias voltage with decreasing V_G. We find the strong dI/dV_S peak is highly polarized on sublattice A_1 because, as can be seen from Fig. 2c, the strong dI/dV_S peak is absent on sublattice B_1. Notably, this feature has not been seen in previous gate resolved STS studies of ABA TLG.[28,29]

Intrigued by this finding we next performed gate and sublattice resolved STS on the ABA TLG/hBN heterostructure in finite and out of plane magnetic field B. Our aim was to investigate the possibility of valley splitting in this system. We first study the B dependence of the tunneling spectra at a constant V_G. Figure 3a shows the experimentally measured tunneling spectra on sublattice A_1 at $V_G = 30$ V with different B. The most prominent feature in these data is the strong dI/dV_S peak that splits into two as B is increased. This behavior was also observed at different V_G on sublattice A_1 but not on sublattice B_1 (see supporting information section S4 for additional data). In addition, we found satellite dI/dV_S peaks emerge with lower intensity as B is increased. In contrast to the prominent sublattice dependent peaks, these satellite dI/dV_S peaks were observed at different V_G and on both sublattices. Figure 3b shows the dependence of the peak splitting energy ΔE on B at $V_G = 30$ V. The relationship between ΔE and B is roughly linear.

We then investigated the influence of V_G on the observed peak splitting at a constant B. Figure 3c shows the measured tunneling spectra on sublattice A_1 with $B = 0.4$ T and at different V_G. We find that the split dI/dV_S peaks shift toward positive voltage bias and diminish in intensity with decreasing V_G. These observations are consistent with Fig. 2b where $B = 0$ T. Additionally, we notice ΔE decreases with increasing V_G. To see this more clearly, we extracted ΔE from Fig.

3c for each V_G, this is shown in Fig. 3d. The splitting energy at $B = 0.4$ T decreases from approximately 12 meV to 6 meV with increasing V_G.

The experimental findings in our STS study on ABA TLG/hBN heterostructures can be understood by considering the capacitive coupling between the STM tip and ABA TLG. Previous STS studies on MLG and BLG on hBN demonstrated that a quantum dot (QD) can be induced beneath the STM tip due to the gating effect from the tip.[30,31] For ABA TLG on hBN, we expect a similar effect exists. As a result, an ABA TLG QD will be induced beneath the STM tip as schematized in the upper panel of Fig. 3e. The lower left panel of Fig. 3e depicts the STM tip induced potential well and the gapped MLG bands in ABA TLG. Due to quantum confinement, QD states will emerge in such a potential well. These emerging QD states can explain the strong dI/dV_S peak on sublattice A_1, as seen in Fig. 2b. Furthermore, with increasing V_G, the gap size (Δ) of the effective MLG band increases (see supporting information section S5 for details). Because this increased Δ enhances quantum confinement, a stronger dI/dV_S peak should be observed at higher V_G, in agreement with Figs. 2b and 3c. Without applying a B, the time reversal symmetry of the QD is preserved; therefore, at $B=0$, the QD states are valley degenerate.

By applying an out of plane B, the time reversal symmetry of our ABA TLG QD is broken, thus enabling the splitting of the valley degeneracy. As schematized in Fig. 1c, the topological magnetic moments $M_z(\vec{k}) = \tau \frac{e}{\hbar} \frac{\Delta}{[\Delta/(\hbar v_F)]^2 + 4|\vec{k}|^2}$ (v_F is the Fermi velocity of the MLG bands, $\tau = +1$and -1 for K' and K valley, respectively) of the effective MLG bands in K and K' valleys are both out of plane and with opposite orientations and concentrated at the band edges. Thus, an out of plane B will couple to the opposite $\vec{M} = \hat{z}\tau M_z$ of the electrons in the two valleys and generate valley splitting. This is schematized in the lower right panel of Fig. 3e for our ABA TLG QD state and explains the ΔE seen in our experiment. Using this simple picture, ΔE can be approximated as $2\left|\vec{M} \cdot \vec{B}\right|$, which can also be expressed as $g_v \mu_B B$. Here μ_B is the Bohr magneton, and g_v is defined as the valley g factor. Using this definition, the extracted g_v is plotted in Fig. 3f as a function of the effective MLG band gap size Δ (see supporting information section S5 for Δ extraction at different V_G). The extracted g_v values are shown as red dots and depict an exceptionally large g-factor that can be highly tuned by modulation of an external gate voltage. The combination of these two attributes is unparalleled in previously studied systems.[4,16]

To quantitatively verify the simple picture described above we calculate g_v for a gapped MLG QD. As a starting point for modelling, we employ a tight-binding model for TLG, schematized in Fig. 1a. Here, we map the antisymmetric wavefunction combination of sublattices A_1 and A_3 (blue shading) and B_1 and B_3 (orange shading) onto a new sublattice A and B of an effective MLG lattice. This effective MLG lattice gives rise to effective MLG bands.[25] Because of the energy difference between γ_2 and γ_5 hopping terms, and the onsite energy difference between the trimer and non-trimer sites (Δ_{AB}), the effective MLG sublattices have different energies, leading to a light-mass Dirac spectrum. A full tight-binding calculation of the ABA TLG band structure in the absence of a perpendicular electric field is plotted in Fig. 1c, where the effective MLG and BLG bands (both gapped) are indicated by the blue cones and semi-transparent red shells. Here, it is important to note that the effective MLG band gap depends on the out-of-plane electric field, E_z, giving rise to a tunable topological magnetic moment. This gap can be expressed as $\Delta = \frac{1}{2}\sqrt{\gamma_2^2 + (U_1 - U_3)^2} + \frac{\gamma_5}{2} - \Delta_{AB}$, where $U_1 - U_3 \propto E_z$ is the interlayer energy difference between the top and bottom layer of ABA TLG. Modulation of this quantity *via* an external electric field controls the intensity of inversion symmetry breaking. As shown in Fig. 1b, by increasing the MLG gap from 14 meV to 26 meV, the maximum value of the topological magnetic moment changes from $808\mu_B$ to $442\mu_B$.

With the 'bulk' 2D properties of TLG bands fully quantified using the fully parametrized Hamiltonian for the low-energy TLG states, we compute the form of electronic wave functions, confined by the QD (created by the tip potential and image charges). Then we use plane wave representation $\psi(\vec{k})$ of the QD states at $B = 0$ T to estimate the effective valley g-factor, $g_v = \frac{2}{\mu_B}\int M(\vec{k})\left|\psi(\vec{k})\right|^2 d\vec{k}$, (see supporting information S6 for details of the calculation) which also describes the computed evolution of the dot spectra as a function of B. The results of such an analysis is shown as a blue solid line in Fig. 3f, displaying a good agreement with the experimental data, both in terms of the observed trend and values. From this, we conclude the large values of g_v, observed in the experiment, are due to the topological magnetic moments in the effective MLG bands of ABA TLG.

In addition, we performed numerical calculation of the local density of states in a tight binding (TB) model for a full ABA TLG quantum dot Hamiltonian. The details of this calculation can be found in supporting information section S6. The simulated local density of states (LDOS) on sublattice A_1 with $V_G = 30$ V and at different B are shown in Fig. 4a. A pronounced LDOS peak appearing at $E = -25\ meV$ corresponds to a localized valence band state of MLG trapped in the hole-doping tip potential. The splitting of this peak under a finite B can be viewed as a splitting between the valence band Landau levels 0 and -1 in the presence of the trapping potential with a splitting energy similar to that shown in Fig. 3a (see supporting information S6 for details). Also, in Fig. 4b, we show the simulated LDOS on sublattice A_1 in $B = 0.4$ T and at different V_G. Here the reduction of ΔE with increasing V_G is reproduced in agreement with Fig. 3c. In addition, from Fig. 4b we extracted g_v by using $\Delta E = g_v \mu_B B$ and plotted these values in Fig. 3f confirming the estimations made using a simplified gapped MLG QD model.

For a more detailed analysis, we compare simulated $LDOS(E,B)$ and measured $dI/dV_S(V_S,B)$ at $V_G = 30$ V for the two sublattices. On sublattice A_1, the split peaks associated with valley splitting appeared in both simulation (Fig. 4c) and experiment (Fig. 4e). Whereas on sublattice B_1, the split peaks are absent in both simulation (Fig. 4d) and experiment (Fig. 4f). In addition, both simulations and experiments show satellite peaks on sublattice A_1 and sublattice B_1 with nonuniform energy spacing. The latter feature is characteristic of MLG Landau levels.[32] Finally, we noticed there is a discrepancy between the simulation and experiment for the LDOS on sublattice B_1, for which simulation predict a stronger peak at $E \approx -25$ meV than observed in the experiment.

In conclusion, we fabricated high quality ABA TLG/hBN heterostructure devices and studied their gate and sublattice resolved tunneling spectra in perpendicular electric and magnetic fields. Our work shows that the effective MLG bands of ABA TLG host giant and gate tunable topological magnetic moments that can generate large and tunable valley splitting in a small B. These findings demonstrate that ABA TLG is a unique platform for fabricating valley-based quantum information devices and studying topological magnetic moment related phenomena.

Acknowledgments: We acknowledge useful discussions with Angelika Knothe, Pablo Perez Piskunow, and Joseph Weston. J.V.J. and Z.G. acknowledges support from the National Science Foundation under award DMR-1753367. J.V.J acknowledges support from the Army Research Office under contract W911NF-17-1-0473. V.F. and S.S. acknowledge support from the European Graphene Flagship Core 3 Project. V.F. acknowledges support from Lloyd Register Foundation Nanotechnology Grant, EPSRC grants EP/V007033/1, EP/S030719/1 and EP/N010345/1. K.W. and T.T. acknowledge support from the Elemental Strategy Initiative conducted by the MEXT, Japan, Grant Number JPMXP0112101001, JSPS KAKENHI Grant Numbers JP20H00354 and the CREST(JPMJCR15F3), JST.

Figure 1

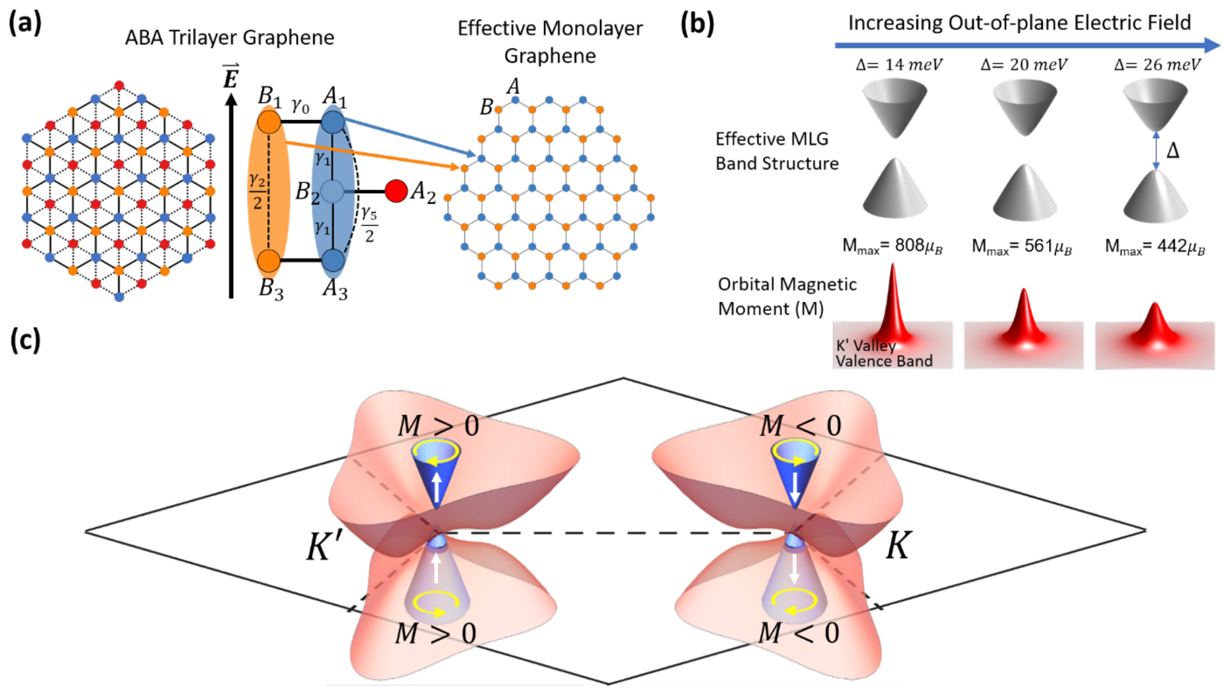

Figure1: Effective MLG band in ABA TLG with giant and tunable topological magnetic moment. **a,** Left panel: Top view of the ABA TLG atomic structure. Middle panel: Schematic of the ABA TLG unit cell with γ_0, γ_1, γ_2 and γ_5 hopping parameters. Right panel: Mapping of the antisymmetric wavefunction combination of sublattices A_1 and A_3 (B_1 and B_3) in ABA TLG onto sublattice A (B) of the effective MLG lattice. **b,** Upper panel: Low energy band structures of the effective gapped MLG with different out-of-plane electric fields applied to the ABA TLG. Lower panel: Topological magnetic moment in the K' valley valence band of the corresponding gapped MLG bands shown in the upper panel. **c,** Schematic of the calculated low energy band structure of ABA TLG with no external electric field in K and K' valleys. Blue cones represent the effective MLG bands. The semi-transparent red shells represent the effective BLG bands. The yellow arrows depict the orientation of the self-rotating wave packet in each band and the white arrows for each band correspond to the sign and direction of the topological magnetic moment originating from the self-rotating wave packet.

Figure 2

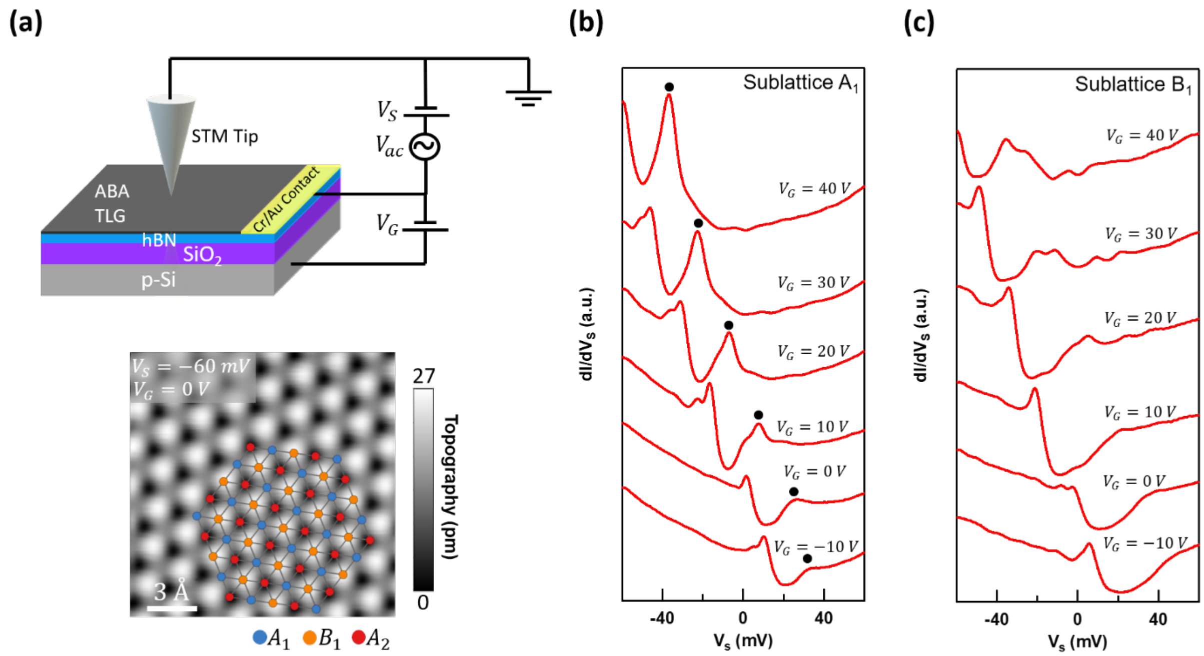

Figure 2: Atomically resolved scanning tunneling spectroscopy (STS) of ABA TLG. a, Upper panel: Schematic of the experimental setup. The ABA TLG/hBN heterostructure rests on a SiO_2/Si substrate and ABA TLG is contacted *via* a Cr/Au electrode. The STM tip is grounded, a bias voltage V_S is applied between the STM tip and ABA TLG. A backgate voltage V_G is applied between the p-doped silicon and ABA TLG. Lower panel: Atomically resolved topography of a pristine ABA TLG patch at $V_G = 0\ V$, the scanning parameters used are $I = 1$ nA, $V_S = -60$ mV. The ABA TLG atomic structure is overlaid on top of the topography, the definition of the sublattice is consistent with that in Fig. 1a and 1b. **b-c,** Tunneling spectra at various gate voltages on sublattice A_1 **(b)** and B_1 **(c)**. At high V_G, a sharp dI/dV_S peak emerges on sublattice A_1 (marked by a black dot). Notably, this dI/dV_S peak is not apparent on sublattice B_1. The set point used to acquire the tunneling spectra was $I = 1$ nA, $V_S = -60$ mV, with a 2 mV ac modulation.

Figure 3

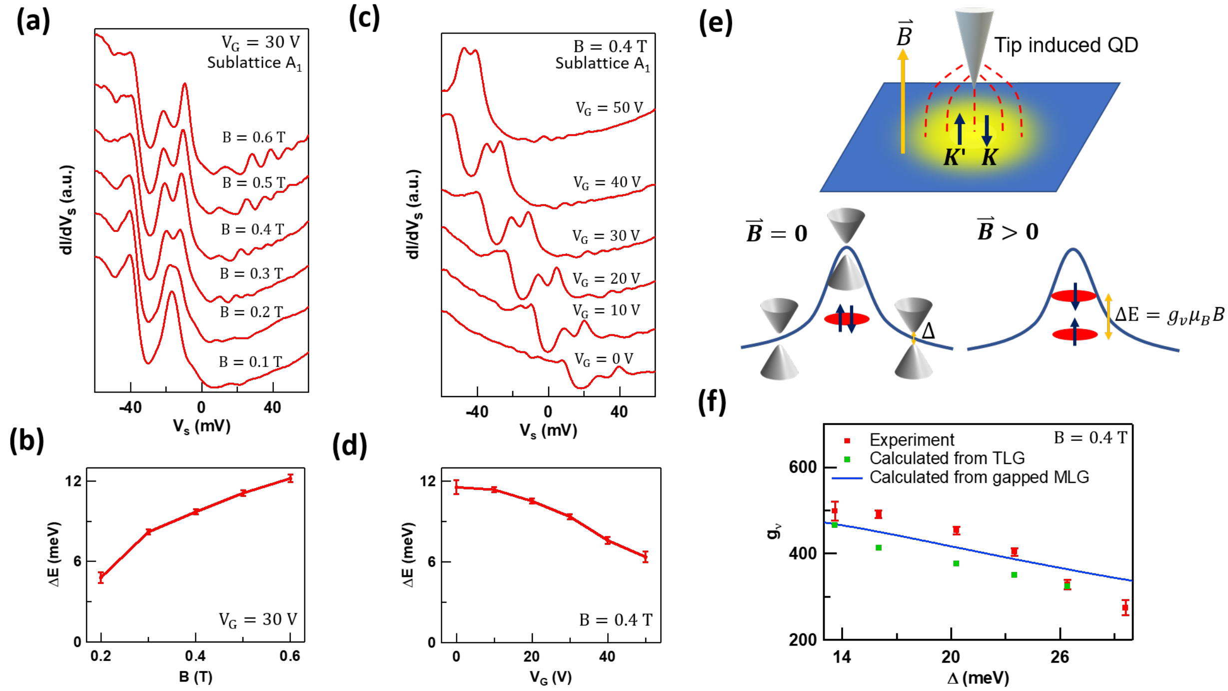

Figure 3: Magnetic field-controlled valley splitting and giant gate tunable valley g factor in ABA TLG. a, Tunneling spectra on sublattice A₁ at $V_G = 30$ V with different out-of-plane magnetic fields (B). The set point used to acquire the tunneling spectra was $I = 1$ nA, $V_S = -60$ mV, with a 2 mV ac modulation. **b,** Extracted splitting energies at $V_G = 30$ V from **a** under different B. **c,** Tunneling spectra on sublattice A₁ at $B = 0.4$ T with different V_G. The set point used to acquire these tunneling spectra was $I = 1$ nA, $V_S = -60$ mV, with a 2 mV ac modulation. **d,** Extracted splitting energies at $B = 0.4$ T from **c** under different V_G. **e,** Upper panel: Schematic of an electric field induced quantum dot (QD) on ABA TLG by the STM tip. The black arrows represent the direction of the orbital magnetic moments in the TLG K and K' valleys, which couple to the external B (orange arrow). Lower left panel: Schematic of the tip induced QD potential profile. The blue line represents the CNP of gapped MLG, the red oval schematizes the QD state arising from confinement. The black arrows represent the degenerate valley degree of freedom.

Lower right panel: Schematic of QD state valley splitting under a B. **f,** Comparison between the experimentally extracted and theoretically calculated valley g factor g_v at $B = 0.4$ T with different gap sizes for the effective MLG band. The continuous line is calculated from a gapped MLG model with a gaussian shaped QD wavefunction. The blue dots represent the simulated g_v from a full tight binding ABA TLG QD model.

Figure 4

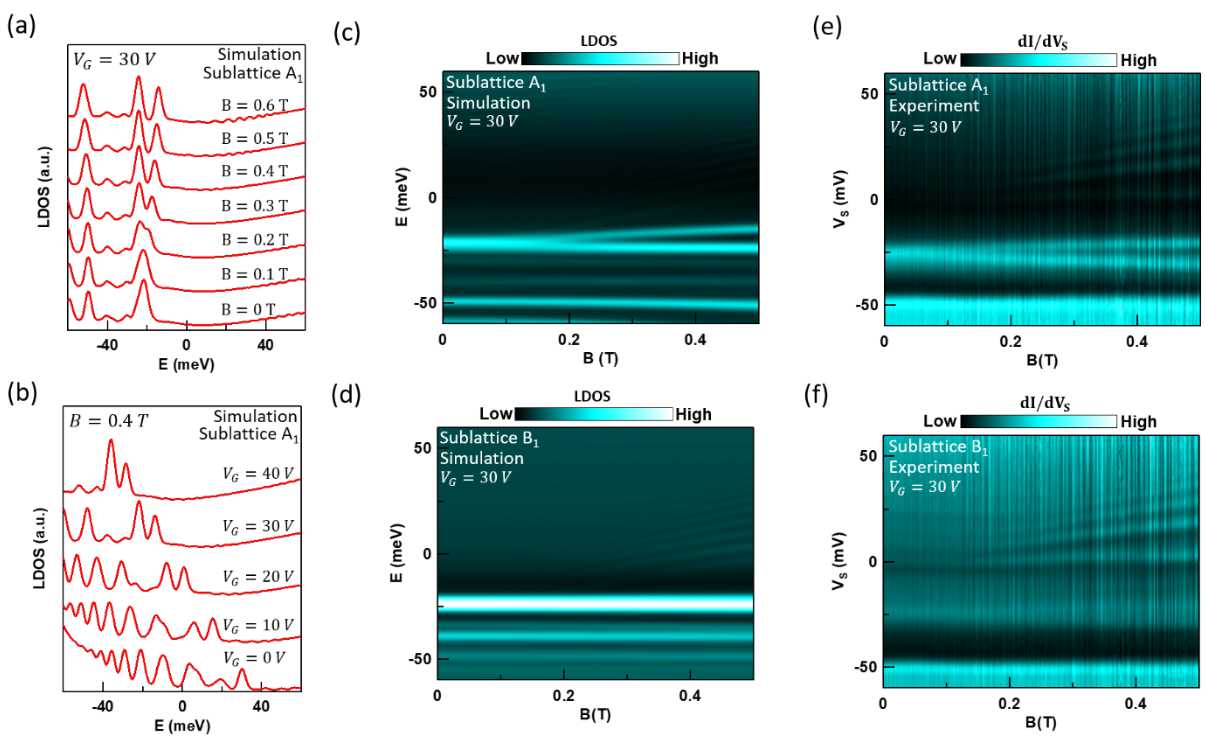

Figure 4: Tight binding LDOS simulation for an ABA TLG QD in *B*. a, Simulated LDOS on sublattice A1 for an ABA TLG QD at $V_G = 30$ V under various B fields. **b,** Simulated LDOS on sublattice A1 for an ABA TLG QD under $B = 0.4$ T with various applied V_G. **c-d,** Simulated $LDOS(E, B)$ color plots on sublattice A1 **(c)** and B1 **(d)** for an ABA TLG QD at $V_G = 30$ V. **e-f,** Experimentally measured $dI/dV_S(V_S, B)$ color plots on sublattice A1 **(e)** and B1 **(f)** at $V_G = 30$ V. The tunneling spectra were measured with a different calibrated STM tip and from a different

location on the sample compared to the data presented in Fig. 3. The set point used to acquire the tunneling spectra was $I = 1$ nA, $V_S = -60$ mV, with a 2 mV ac modulation.

References

1 Xiao, D., Yao, W. & Niu, Q. Valley-contrasting physics in graphene: magnetic moment and topological transport. *Physical Review Letters* **99**, 236809 (2007).

2 Wu, S. *et al.* Electrical tuning of valley magnetic moment through symmetry control in bilayer MoS 2. *Nature Physics* **9**, 149-153 (2013).

3 Aivazian, G. *et al.* Magnetic control of valley pseudospin in monolayer WSe 2. *Nature Physics* **11**, 148-152 (2015).

4 Komatsu, K. *et al.* Observation of the quantum valley Hall state in ballistic graphene superlattices. *Science advances* **4**, eaaq0194 (2018).

5 Overweg, H. *et al.* Topologically nontrivial valley states in bilayer graphene quantum point contacts. *Physical review letters* **121**, 257702 (2018).

6 Moriya, R. *et al.* Emergence of orbital angular moment at van Hove singularity in graphene/h-BN moiré superlattice. *Nature communications* **11**, 1-6 (2020).

7 Li, Y. *et al.* Valley splitting and polarization by the Zeeman effect in monolayer MoSe 2. *Physical review letters* **113**, 266804 (2014).

8 MacNeill, D. *et al.* Breaking of valley degeneracy by magnetic field in monolayer MoSe 2. *Physical review letters* **114**, 037401 (2015).

9 Srivastava, A. *et al.* Valley Zeeman effect in elementary optical excitations of monolayer WSe 2. *Nature Physics* **11**, 141-147 (2015).

10 Freitag, N. M. *et al.* Electrostatically confined monolayer graphene quantum dots with orbital and valley splittings. *Nano letters* **16**, 5798-5805 (2016).

11 Eich, M. *et al.* Spin and valley states in gate-defined bilayer graphene quantum dots. *Physical Review X* **8**, 031023 (2018).

12 Freitag, N. M. *et al.* Large tunable valley splitting in edge-free graphene quantum dots on boron nitride. *Nature nanotechnology* **13**, 392-397 (2018).

13 Kraft, R. *et al.* Valley Subband splitting in bilayer graphene quantum point contacts. *Physical review letters* **121**, 257703 (2018).

14 Kurzmann, A. *et al.* Excited states in bilayer graphene quantum dots. *Physical review letters* **123**, 026803 (2019).

15 Wang, T. *et al.* Giant valley-Zeeman splitting from spin-singlet and spin-triplet interlayer excitons in WSe2/MoSe2 heterostructure. *Nano letters* **20**, 694-700 (2019).

16 Lee, Y. *et al.* Tunable valley splitting due to topological orbital magnetic moment in bilayer graphene quantum point contacts. *Physical review letters* **124**, 126802 (2020).

17 Lu, X. *et al.* Superconductors, orbital magnets and correlated states in magic-angle bilayer graphene. *Nature* **574**, 653-657 (2019).

18 Sharpe, A. L. *et al.* Emergent ferromagnetism near three-quarters filling in twisted bilayer graphene. *Science* **365**, 605-608 (2019).

19 He, W.-Y., Goldhaber-Gordon, D. & Law, K. T. Giant orbital magnetoelectric effect and current-induced magnetization switching in twisted bilayer graphene. *Nature communications* **11**, 1-8 (2020).

20 Polshyn, H. *et al.* Electrical switching of magnetic order in an orbital Chern insulator. *Nature* **588**, 66-70 (2020).

21 Zhu, J., Su, J.-J. & MacDonald, A. H. Voltage-Controlled Magnetic Reversal in Orbital Chern Insulators. *Physical Review Letters* **125**, 227702 (2020).

22 Lee, Y. *et al.* Tunable Valley Splitting due to Topological Orbital Magnetic Moment in Bilayer Graphene Quantum Point Contacts. *Physical Review Letters* **124**, 126802, doi:10.1103/PhysRevLett.124.126802 (2020).

23 Taychatanapat, T., Watanabe, K., Taniguchi, T. & Jarillo-Herrero, P. Quantum Hall effect and Landau-level crossing of Dirac fermions in trilayer graphene. *Nature Physics* **7**, 621-625 (2011).

24 Zomer, P., Dash, S., Tombros, N. & Van Wees, B. A transfer technique for high mobility graphene devices on commercially available hexagonal boron nitride. *Applied Physics Letters* **99**, 232104 (2011).

25 Koshino, M. & McCann, E. Gate-induced interlayer asymmetry in ABA-stacked trilayer graphene. *Physical Review B* **79**, 125443 (2009).

26 Que, Y. *et al.* Stacking-dependent electronic property of trilayer graphene epitaxially grown on Ru (0001). *Applied Physics Letters* **107**, 263101 (2015).

27 Zhang, Y., Qiao, J.-B., Yin, L.-J. & He, L. High-resolution tunneling spectroscopy of ABA-stacked trilayer graphene. *Physical Review B* **98**, 045413 (2018).

28 Yankowitz, M., Wang, F., Lau, C. N. & LeRoy, B. J. Local spectroscopy of the electrically tunable band gap in trilayer graphene. *Physical Review B* **87**, 165102 (2013).

29 Yankowitz, M. *et al.* Electric field control of soliton motion and stacking in trilayer graphene. *Nature materials* **13**, 786-789 (2014).

30 Zhao, Y. *et al.* Creating and probing electron whispering-gallery modes in graphene. *Science* **348**, 672-675 (2015).

31 Liu, Y.-W., Hou, Z., Li, S.-Y., Sun, Q.-F. & He, L. Movable Valley Switch Driven by Berry Phase in Bilayer-Graphene Resonators. *Physical review letters* **124**, 166801 (2020).

32 Luican, A., Li, G. & Andrei, E. Y. Quantized Landau level spectrum and its density dependence in graphene. *Physical Review B* **83**, 041405, doi:10.1103/PhysRevB.83.041405 (2011).